

Journal of Biomedical Optics

SPIEDigitalLibrary.org/jbo

Review of speckle and phase variance optical coherence tomography to visualize microvascular networks

Mohammad Sultan Mahmud
David W. Cadotte
Barry Vuong
Cary Sun
Timothy W. H. Luk
Adrian Mariampillai
Victor X. D. Yang

Review of speckle and phase variance optical coherence tomography to visualize microvascular networks

Mohammad Sultan Mahmud,^d David W. Cadotte,^{b,c} Barry Vuong,^a Carry Sun,^a Timothy W. H. Luk,^a Adrian Mariampillai,^{a,c} and Victor X. D. Yang^{a,b,d,e,f}

^aRyerson University, Biophotonics and Bioengineering Laboratory, 350 Victoria Street, Toronto, Ontario M5B 2K3, Canada

^bUniversity of Toronto, Division of Neurosurgery, Department of Surgery, Toronto, Canada

^cUniversity Health Network, Krembil Neuroscience Center, Toronto Western Hospital, Toronto, Canada

^dRyerson University, Department of Electrical and Computer Engineering, 350 Victoria Street, Toronto, Ontario M5B 2K3, Canada

^eSunnybrook Health Sciences Centre, Division of Neurosurgery, Department of Surgery, Toronto, Canada

^fSunnybrook Research Institute, Imaging Research, Toronto, Canada

Abstract. High-resolution mapping of microvasculature has been applied to diverse body systems, including the retinal and choroidal vasculature, cardiac vasculature, the central nervous system, and various tumor models. Many imaging techniques have been developed to address specific research questions, and each has its own merits and drawbacks. Understanding, optimization, and proper implementation of these imaging techniques can significantly improve the data obtained along the spectrum of unique research projects to obtain diagnostic clinical information. We describe the recently developed algorithms and applications of two general classes of microvascular imaging techniques: speckle-variance and phase-variance optical coherence tomography (OCT). We compare and contrast their performance with Doppler OCT and optical microangiography. In addition, we highlight ongoing work in the development of variance-based techniques to further refine the characterization of microvascular networks. © The Authors. Published by SPIE under a Creative Commons Attribution 3.0 Unported License. Distribution or reproduction of this work in whole or in part requires full attribution of the original publication, including its DOI. [DOI: [10.1117/1.JBO.18.5.050901](https://doi.org/10.1117/1.JBO.18.5.050901)]

Keywords: speckle-variance optical coherence tomography; phase-variance optical coherence tomography; microcirculation; Doppler optical coherence tomography; optical microangiography; bulk tissue motion; photodynamic therapy.

Paper 12748VR received Nov. 20, 2012; revised manuscript received Mar. 14, 2013; accepted for publication Mar. 19, 2013; published online Apr. 24, 2013.

1 Introduction

Over the last decade, various techniques have been reported to image microvascular networks, whose aims range from distinct research questions to the diagnosis and monitoring of specific pathologies. Color fundus photography, fluorescein angiography (FA), and indocyanine green angiography served as standard methods for imaging the retinal vascular structure.¹ These imaging techniques require the injection of exogenous contrast agents into the circulation, which may cause allergic reaction. Moreover, these techniques cannot provide blood vessel depth information and are limited by the two-dimensional (2-D) nature of the images.

An attractive optical technique for imaging three-dimensional (3-D) microvasculature structure without the need of exogenous agents is vascular-sensitive optical coherence tomography (OCT). The OCT technique is based on the principle of low-coherence interferometry, and it offers the advantages of being noninvasive, contactless, and yields depth-resolved localization at high spatial and temporal resolutions cross-sectional imaging in biological systems. cross-sectional imaging in biological system.^{2,3} Moreover, intrinsic contrast mechanisms and depth resolution of tissue are advantages over confocal fluorescence microscopy. Unlike the sound echoes of ultrasound, OCT generates images based upon back-reflected light from the sample. Various OCT blood flow detection techniques have been

developed for imaging vasculature structure, each of which has its own merits and drawbacks. For example, Doppler OCT⁴⁻¹⁵ (also known as optical Doppler *tomography*), images are reconstructed based on phase changes or Doppler frequency shifts due to moving particles in the sample. Phase changes are calculated from multiple axial scans (A-scans) collected at the same position, or adjacent A-scans with sufficient spatial overlap. The DOCT method is useful in mapping blood vessels in various tissue such as skin^{16,17} and retina¹⁸ and can extract blood-flow information. Several useful strategies such as dual-beam DOCT¹⁹⁻²¹ and narrow bandwidth phase-reference OCT,²² are reported to improve the sensitivity of DOCT. All of these methods are phase-sensitive, and therefore a phase-stable system is necessary for obtaining high-contrast images.²³

The power Doppler OCT and/or optical angiography/microangiography (OMAG) are other imaging techniques based on the Doppler effect that is able to isolate blood flow signals from the static tissue background.²⁴⁻³⁶ This method does not allow visualization of flow velocity directly; it provides a measure of the total backscattered optical signal attributable to moving targets with higher SNR³⁷ compared to DOCT. Unlike phase-based approaches, OMAG directly analyzes and processes an image, which can minimize the phase instability noise. Different phase compensation methods³⁷⁻³⁹ were introduced to compensate motion artifacts from OMAG measurement. Overall real-time application of power Doppler or OMAG is computationally intensive and may require graphics processing unit (GPU)-based signal processing techniques to clinical suitability.

Two recently developed high-contrast *in vivo* 2-D/3-D microcirculation imaging techniques, with various implementations

Address all correspondence to: Victor X. D. Yang, Ryerson University, Biophotonics and Bioengineering Laboratory, 350 Victoria Street, Toronto, Ontario M5B 2K3, Canada. Tel: 416-803-9320; Fax: 416-979-5280; E-mail: yangv@ee.ryerson.ca

by research groups, are speckle-variance (SV) and phase-variance (PV) OCT. SV-OCT images microvasculature by calculating the interline or interframe speckle variance of the intensity-based structural OCT images.⁴⁰⁻⁴⁶ The calculation of the variance of the signal intensity is determined either by a spatial window⁴⁰ or temporal window.^{41,42} The spatial window method uses the speckle of the conventional structural OCT images.⁴⁰ However, the performance of this system is hindered by the computational complexity and slow frame rate in the initial demonstration.⁴¹ Developments of high-speed swept-source laser^{16,17} may yield sufficient imaging speed of this technique. The temporal window method^{41,42} is based on calculating the interframe speckle variations between successive structural (B-mode) OCT images. This method provides high-contrast microvasculature images with enhanced sensitivity and angle independence, without the need of a high-phase stability system. However, the images suffer from blood vessel shadowing artifacts^{47,48} and bulk tissue motion.⁴¹ Szkulmowski et al.⁴⁹ averaged the multiple A-scans, and Lee et al.⁵⁰ coded the discrete Fourier transform algorithm to improve the speckle contrast from the OCT images with the capability of real-time signal processing.

The PV-OCT method^{47,51-66} has been implemented to visualize the vasculature of zebrafish,⁵⁹ ocular circulation of the mouse,⁶⁰ and human retinal vasculature.^{47,61-66} This method identifies the phase difference between consecutive B-scans of the same transverse position and allows for the mapping of microvasculature, independent of the direction of flow relative to the imaging system.^{47,60} High-speed phase stable imaging systems and postimage processing can reduce motion artifacts, which may further advance this technique for use in clinical applications.

In this article, we report on the principles, algorithms, current state of the art, and future applications of microvascular imaging based on SV and PV techniques. Studies are ongoing for improving complete microvascular metrics, as well as assessing blood flow information by optimizing system acquisition parameters or by improving the OCT system.

2 Theory

2.1 SV Processing

The term *speckle* is used to describe the OCT signal acquired as a result of partial coherently backscattered light from biological tissues.⁶⁷⁻⁷¹ If an OCT image is acquired in a stationary object, the speckle pattern is temporally stationary as well.⁴⁴ Due to the

presence of moving particles in biological tissues (such as red blood cells), the speckle pattern varies with time and can be quantified by speckle variance calculations using either inter-frame or interline comparisons.

Fundamentally, SV imaging is a decorrelative measurement technique that has the capability to visualize blood flow, independent of the Doppler angle. This method is suitable for detecting small blood vessel networks because of its angle independence and fast image acquisition capability. Decorrelation methods based on speckle intensity variation in B-scan images were previously introduced in ultrasound systems.^{72,73} In OCT, SV imaging has the capability of detecting microvasculature through intrinsic contrast in the scattering properties of red blood cells as they move through the vascular network. These speckle variance images (SV_{ijk}) are created by evaluating variance in the structural pixel intensity (I_{ijk}) across the desired number (N) of B-scan images at the same spatial location using the following equation:

$$\begin{aligned}
 SV_{ijk} &= \frac{1}{N} \sum_{i=1}^N \left[I_{ijk}(x, z) - \frac{1}{N} \sum_{i=1}^N I_{ijk}(x, z) \right]^2 \\
 &= \frac{1}{N} \sum_{i=1}^N (I_{ijk} - I_{\text{mean}})^2.
 \end{aligned} \quad (1)$$

Here, i , j , and k are indices of frame, lateral (or width), and depth (or axial) position (pixels) of the B-scan, respectively; N is the number of frames used in variance calculation (or gate length); $I_{ijk}(x, z)$ is the signal intensity at pixel (j, k) in the i 'th frame; and I_{mean} is the average intensity over the same set of pixels.

The SV estimate from Eq. (1) differs in solid and fluid components of biological tissue, as they have different time-dependent scattering properties, which provide the intrinsic contrast in speckle variance. For example, in the regions of solid tissue, assuming no bulk tissue motion (BTM), the pixel intensities have a Gaussian distribution profile [Fig. 1(a)]. Contrary to this are the fluid components of biological tissue, such as red blood cells traveling through a vessel, where pixel intensities change and lead to a Rayleigh distribution.⁷⁴

As a consequence, the SV contrast between solid and fluid components of biological tissue can affect the accuracy of the measurement. To account for this, the SV SNR between a “fluid” and “solid” pixel is defined as

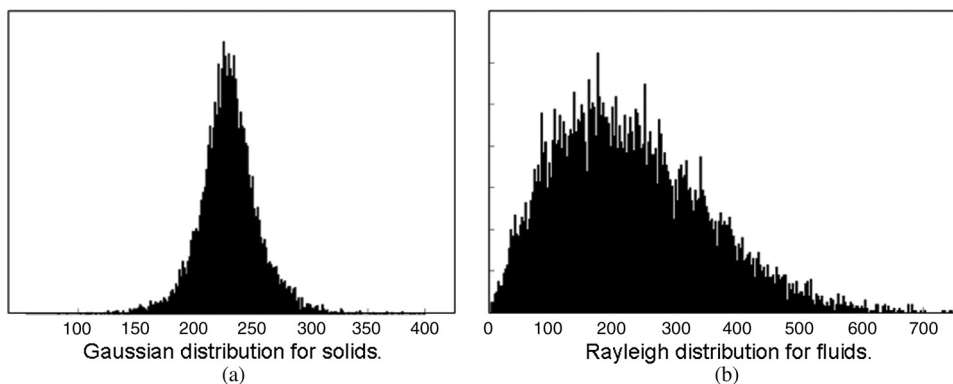


Fig. 1 (a) Gaussian distributions for solids (silicone gel phantom). (b) Rayleigh distribution for fluids (intralipid solution) without bulk motion.⁷⁴

$$SV_{SNR}(N, I_0) = \frac{SV_{Fluid}(N, I_0) - SV_{Solid}(N, I_0)}{\sqrt{\sigma_{Fluid}^2(N, I_0) + \sigma_{Solid}^2(N, I_0)}}, \quad (2)$$

where SV_{Fluid} and SV_{Solid} are the raw SV calculated from Eq. (1); σ_{Fluid}^2 and σ_{Solid}^2 are the variance of SV_{Fluid} and SV_{Solid} , respectively; and I_0 is the equal time-averaged intensity of “fluid” and “solid” pixel. To achieve higher SNR, the gate length (N) was optimized and $N = 8$ was found for lower BTM scenarios.⁴²

A major challenge with using the SV-OCT technique is the effect of blood vessel shadowing artifacts.⁷⁵ The streaking and/or shadowing artifacts encountered as one moves through the blood vessel to the deeper layers of the tissue sample can lead to an overestimation of the vascular area (Fig. 2). To remove these artifacts from the SV image, a step-down exponential filter could be used, while preserving the overall vascular structure.^{11,47,48,75} In this de-shadowing process, the SV signal is attenuated by a factor γ from the top surface of the tissue and is proportional to the sum of the de-shadowed SV pixel above it. Mathematically, the de-shadowing process is expressed as

$$SV_{DS}(x, y, z) = SV(x, y, z) \times e^{\frac{1}{\gamma} \sum_{i=1}^{z-1} SV_{DS}(x, y, i)}, \quad (3)$$

Here, x is the frame, y is the lateral location, z is the depth in each image, and γ is a proportionality constant that controls the rate of attenuation. The de-shadowed imaging scheme shows significantly less shadowing effect than the original B-scan SV image (Fig. 2) and qualitatively found no loss of vascular information due to the overall attenuation of speckle variance intensity (Fig. 3).

Subsequent to the attenuation of the shadowing artifact, a depth-encoding colormap (Fig. 4) is used to preserve vascular depth information in 2-D.⁷⁶ Each image in the stack is first encoded with an RGB color depending on its depth in the stack. The transparency (or alpha channel) for each pixel in the stack is then set to its SV intensity. Both RGB color and alpha channels are then combined to get color depth-encoded SV images.

2.2 PV Processing

An alternative approach for vasculature visualization considers the evaluation of phase change statistics as a contrast mechanism. Various phase-contrast methods, including Doppler imaging and

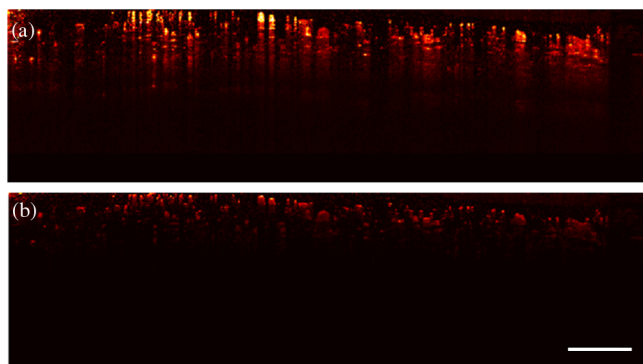


Fig. 2 The B-scan SV image of a tumor microvasculature (a) without de-shadowing (b) with de-shadowing (scale: 1 mm). (Reproduced from Ref. 76 with permission.)

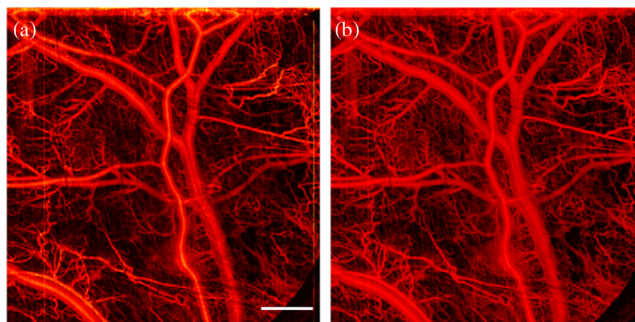


Fig. 3 Projection images of 3-D SV datasets (a) without de-shadowing, (b) with de-shadowing (scale: 1 mm). (Reproduced from Ref. 76 with permission.)

power Doppler tomography (or angiography) and the PV method,^{51,53,55,62} were covered in the introduction. Here, we focus on PV-OCT principles and algorithms as it produces high-contrast microcirculation imaging performance over DOCT and optical microangiography.

PV-OCT utilizes the statistical variance of phase changes over successive OCT scans where phase changes are caused by motion of fluid in vessels or capillaries. It produces high-contrast imaging of 3-D capillary networks. The variance of phase changes can be calculated over successive A-scans during transverse scanning.^{24,36,51–53} The average phase shift ($\Delta\Phi$) between sequential A-scans at the same location (z) is expressed as^{51–53}

$$\begin{aligned} \Delta\Phi(z) &= [\Phi_{j+1,z} - \Phi_{j,z}] \\ &= \tan^{-1} \left\{ \frac{\text{Im} \left[\sum_{j=1}^n (A_{j,z} \cdot A_{j+1,z}^*) \right]}{\text{Re} \left[\sum_{j=1}^n (A_{j,z} \cdot A_{j+1,z}^*) \right]} \right\}, \end{aligned} \quad (4)$$

where $\Phi_{j+1,z}$ and $\Phi_{j,z}$ are the phases for the signal at depth z of the $(j+1)$ 'th and j 'th A-line; $A_{j,z}$ is the complex OCT signal at axial time t and depth z for the j 'th A-line; and n is the number of sequential A-lines that are averaged.

If σ denotes the standard deviation of the Doppler spectrum, the Doppler variance (σ^2) can be derived from autocorrelation technique.^{25,51,77} Usually, averaging is done to improve SNR. The averaging can be performed either in the lateral direction⁵¹ or in both lateral (temporal) and axial (depth) directions.^{24,25,52} Compared to lateral averaging, only Eq. (5), averaging along both the lateral and depth directions [Eq. (6)], can reduce the background noise and improve the image quality.^{25,36}

$$\sigma^2 = \frac{1}{T^2} \left[1 - \frac{\left| \sum_{j=1}^n (A_{j,z} \cdot A_{j+1,z}^*) \right|}{\sum_{j=1}^n (A_{j,z} \cdot A_{j+1,z}^*)} \right] \quad (5)$$

$$\sigma^2 = \frac{1}{T^2} \left[1 - \frac{\left| \sum_{j=1}^n \sum_{z=1}^N (A_{j,z} \cdot A_{j+1,z}^*) \right|}{\sum_{j=1}^n \sum_{z=1}^N (A_{j,z} \cdot A_{j+1,z}^*)} \right]. \quad (6)$$

Here, z represents different data points along each axial scan and j represents different axial scans; T is the time interval between

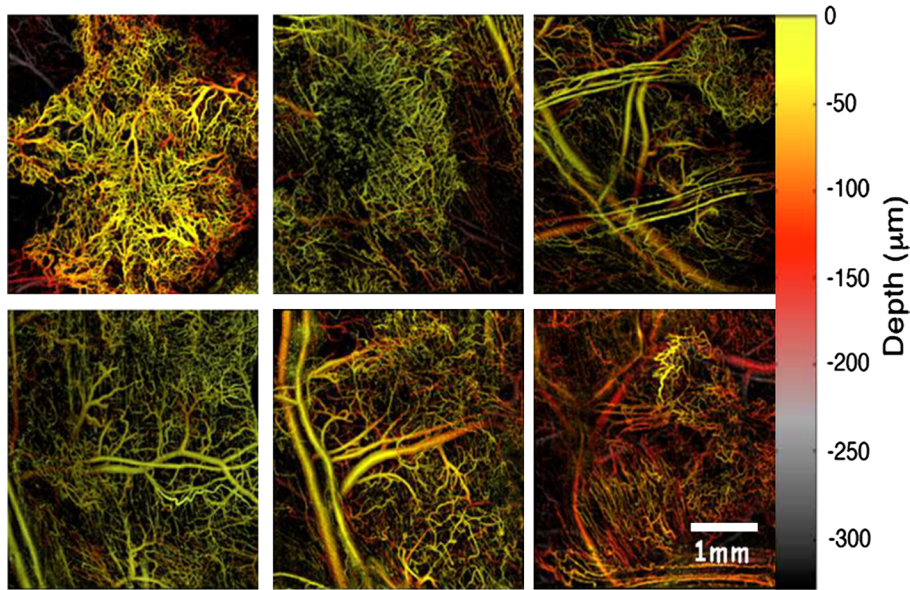


Fig. 4 Depth-encoded SV-OCT images of six window chambers seeded with 9L gliosarcoma tumors imaged nine days after implantation. Features closest to the coverslip are encoded with green-yellow, while deeper features are encoded with orange-red. The transparency of a pixel is determined by the SV intensity. The images show significant amount of intra- and inter-tumor microvascular heterogeneity. (Reprinted from Ref. 76 with permission.)

sequential A-scans; n is the number of A-lines that are averaged; and N is the number of depth points that are averaged. Values of n and N are application dependent. Generally, a larger n and N will increase SNR, but they also increase computation time and decrease resolution.

Phase variance can also be calculated from phase changes between B-scans, where multiple B-scans are required over the same transverse scan.^{61,78} Thus, multiple phase measurements are recorded over the same transverse point separated in time. The phase differences between adjacent frames of the same transverse points can then be obtained, and the variance of these changes can be calculated. The phase difference ($\Delta\Phi$) between two consecutive B-scans at the same location is mathematically expressed as

$$\Delta\Phi(x, z, T) = \Phi_{i+1}(x, z, t + T) - \Phi_i(x, z, t), \quad (7)$$

where $\Phi_i(x, z, t)$ is the phase value in the B-scan at lateral location x , depth position z , and time t ; T is the time interval between two consecutive B-scans; i is an index of i th B-scan within one BM-scan. The phase variance between two consecutive B-scans is calculated as

$$\sigma_{\Delta\Phi}^2 (= PV_{ijk}) = \frac{1}{N-1} \sum_{i=1}^{N-1} \left[\Delta\Phi_i(x, z, t) - \frac{1}{N-1} \sum_{i=1}^{N-1} \Delta\Phi_i(x, z, t) \right]^2, \quad (8)$$

where N represents the number of B-scans and $\Delta\Phi(x, z)$ is the phase difference between two consecutive B-scans.

There are three basic steps in PV-OCT measurement: OCT data acquisition, phase change calculation, and phase variance calculation. Fingler et al.⁵⁹ proposed two different scan mechanisms, MB-scan and BM-scan, to acquire 2-D OCT images with a variety of time separations between phase measurements.

MB-scan takes multiple M-scans over different transverse positions; on the other hand, multiple B-scans over time at the same transverse scan position are referred to as *BM-scans*. Densely sampled A-scans may be required to improve the transverse resolution. It was demonstrated that the phase contrast calculation through an MB-scan could allow cancellation of phase noise-induced error. Unfortunately, MB-scans are time consuming and limit the speed of 2-D phase contrast imaging. On the other hand, BM-scans are more time efficient and commonly used. Additional steps of phase error reduction are needed ultimately to improve the accuracy of PV measurement.⁵⁹

To improve the measurement accuracy, image processing techniques are applied during the PV-OCT procedure. First, to improve the accuracy of phase change calculation, the bulk motion along the imaging direction-induced artifact needs to be compensated. Bulk motion within each frame can be removed by using the Doppler shifts between adjacent A-lines, whereas bulk motion between adjacent frames can be removed by correlation-based algorithms. Fingler et al.⁵⁹ introduced a weighted mean technique that utilizes phase changes from all depths within a chosen region of the A-scan to calculate the bulk motion. The phase change is then corrected by subtracting the tissue motion as

$$\Delta\phi_c(z, T) = \Delta\phi(z, T) - \Delta\phi_{\text{bulk}}(T), \quad (9)$$

where $\Delta\phi_c(z, T)$ is the corrected phase change measured at a given depth z and T is the time separation. Phase variance can then be calculated from the corrected phase change $\Delta\phi_c(z, T)$. The measured variance of motion increases with the time separation between phase measurements T . Histogram-based methods^{47,75,79} are often used to remove phase shifts caused by bulk motion (e.g., eye motion). Liu et al.^{36,80} showed an intensity-based Doppler variance method that is insensitive to bulk motion and can be used without the removal of bulk motion.

We have outlined the principles and algorithms of SV and PV techniques in the above sections. In the following sections, we outline specific applications of SV- and PV-OCT microvascular imaging, putting particular emphasis on the broad application of high-resolution methods to address specific research questions.

3 Applications

Over the past several years, SV- and PV-OCT has been applied to a variety of preclinical and clinical scenarios requiring high-resolution imaging of the microvasculature. In this section, we summarize these applications and highlight both the diversity of use and limitations of these technologies. To begin, we highlight the study of tumor biology, as this was the first reported use of SV-OCT in the literature. Following this introduction, we highlight a variety of applications, including imaging the embryo, applications for the study of neuroscience and ophthalmology, and imaging nanoparticles, and conclude with methodological developments that aim to improve certain aspects of SV-OCT imaging across disciplines. In the second part of this section, we highlight applications of the PV-OCT technique.

3.1 Applications of SV-OCT

3.1.1 Imaging of tumor biology

Mariampillai et al.^{41,42} successfully demonstrated the SV technique to image microvasculatures in animal skin using a window chamber model (Fig. 5). The technique provides Doppler angle-independent microvessel imaging, which overcame the limitation of the DOCT technique.⁹ In the initial work, the smallest detectable microvessels by SV imaging was in the range of 25 μm .⁴¹ One major limitation highlighted by the authors is bulk tissue motion, which prompted further work to improve SV imaging using a different scanning pattern to improve

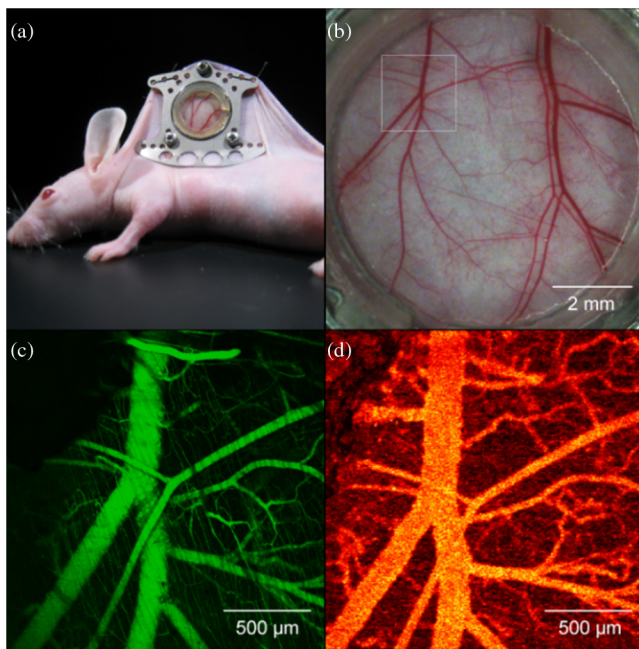


Fig. 5 SV-OCT platform for detection of the microvasculature (a) Dorsal skin fold window chamber model. (b) White light microscopy image of the entire window. The white box represents the confocal fluorescence and SV-OCT imaging locations. (c) Maximum intensity projection image of FCM. (d) SV-OCT *en face* projection image of vasculature. (Reprinted from Ref. 41 with permission.)

imaging speed and SV contrast.⁴² In addition to 2-D imaging, the SV vasculature map can be color-coded¹¹ according to the depth of vessels in the tissue (Fig. 6). Unlike the structural OCT image [Fig. 6(a)], satellite metastases are clearly observed in SV images, as indicated with blue arrows in Fig. 6(b). Significant improvement of microvessel contrast was found when the number of frames (N) increased from 2 to 8. The SV approach showed better performance for detecting microvasculature over color DOCT, due to its sensitivity and angle independence; however, it still suffers from blood vessel shadowing artifacts.^{47,48}

To detect locations of retinal microvasculature and assess blood oxygen level effectively, Liu et al.⁴⁴ combined speckle variance with spectroscopic OCT (SOCT) techniques. The SV-OCT images were calculated [from Eq. (1)] and compared the effect of using different numbers of frames ($N = 10, 100,$ and 500) of OCT images processed. Large numbers of frames required can increase image acquisition and data processing time. Simple thresholding when applied in the SV images could allow determination of the location and dimension of the capillary blood vessels [Fig. 7(d)]. The SOCT image was then combined with the thresholded SV-OCT image to determine the spectroscopic properties of blood vessels, such as blood oxygen level and speckle noise, based on the attenuation properties of the blood in different wavelength ranges and the results are shown in Fig. 7(e) and 7(f). The spatial variations of blood vessels were represented by the full dynamic range of color code; red and purple represent the minimum and maximum speckle variance in the blood vessels. The combined results showed the localized spectroscopic properties of the blood microvascular structure with future potential of functional OCT imaging applications.

A better understanding of structural and functional properties of tumor microcirculation can potentially contribute to monitoring, preventing, and improving the treatment of tumor or cancer therapies. Formation of new vessels, remodeling, and dropout of exiting vessels inside a tumor can continuously create temporal variations in blood flow and oxygenation.⁶⁶ For the study of tumor hemodynamic, Skala et al.⁸¹ combined the hyperspectral

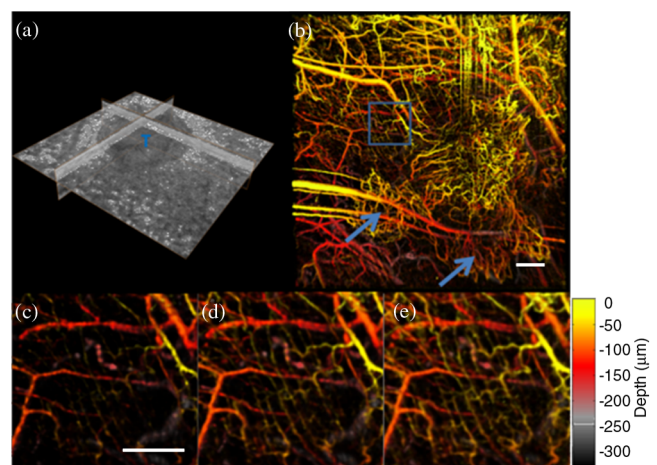


Fig. 6 (a) Structural image of a tumor. (b) Microvascular projection image for the tumor, with gate length $N = 8$. Arrows indicate the location of satellite metastasis. The color indicates relative depth of the vessels, with brighter shades indicating superficial (closest to the cover slip of the window chamber) and gray indicating deeply seated vasculature (c)–(e). Magnified region shows the effects of increased frames ($N = 2, 4, 8$). Scale bar: 250 μm . (Reprinted from Ref. 42 with permission.)

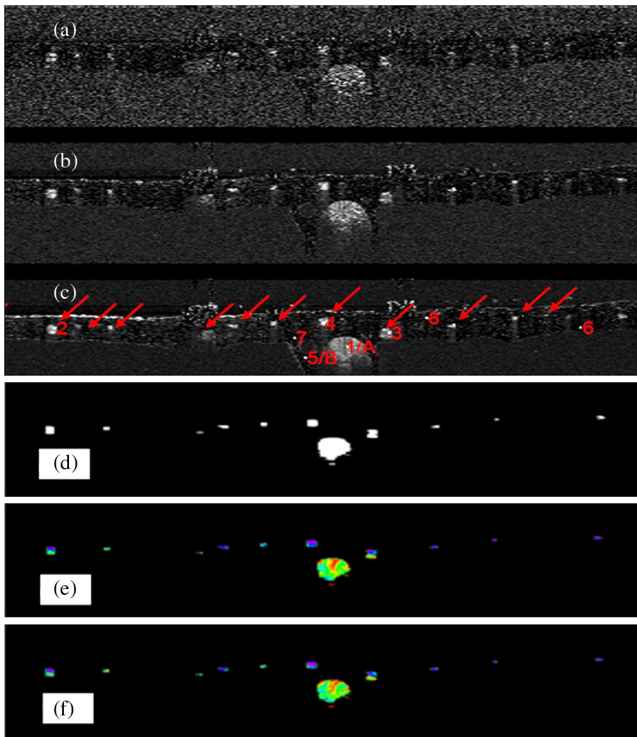


Fig. 7 SV-OCT images obtained for image frame (a) $N = 10$, (b) $N = 100$, and (c) $N = 500$. The positions of capillary blood vessels, indicated as red arrows. (d) Threshold SV-OCT image that highlights blood vessels, (e) Combined SV-OCT and SOCT image were obtained from short time Fourier transform (STFT) method, and (f) Combined SV-OCT and SOCT image obtained via the two-wavelength method. (Reproduced from Ref. 44 with permission.)

imaging with Doppler and SV-OCT to noninvasively microvasculature, hemoglobin oxygen saturation level (SO_2), flow information, and shear rate on the vessel wall with tumor growth (Fig. 8). Eight repeated B-scans were used to collect SV-OCT images, whereas for DOCT images, 10 repeated A-scans were used. Combining such measurements reveal potential for clinical applications requiring detection of flow velocity, vessel diameter and morphology, as well as oxygen saturation level inside tumors, which can be determined accurately without the use of contrast agents.

The SV-OCT technique can also be used to monitor the change of tissue properties during photodynamic therapy (PDT) and radiation-based cancer treatments.^{41,82–84} Mariampillai et al.⁴¹ showed the detection of microvascular changes induced by PDT before, during, and immediately after posttreatment. The smaller blood vessels disappeared approximately 1 min after the PDT laser exposure [Fig. 9(b)]. A transient complete shutdown of one of the larger vessels occurred between 5 min, 40 s, and 6 min, 35 s, with a partial reperfusion event at 6 min, 27 s [Fig. 9(c)–9(e)]. At the end of the PDT laser irradiation, the smaller vessels were completely closed, whereas the larger vessels had an approximately 30% reduction of diameter as measured by the SV-OCT technique [Fig. 9(f)].

3.1.2 Imaging oral tissue

Davoudi et al.⁸⁵ reported 3-D microstructural morphology and compared images of healthy [Fig. 10(a)] and scar regions [Fig. 10(b)] in the human oral cavity using the SV technique.

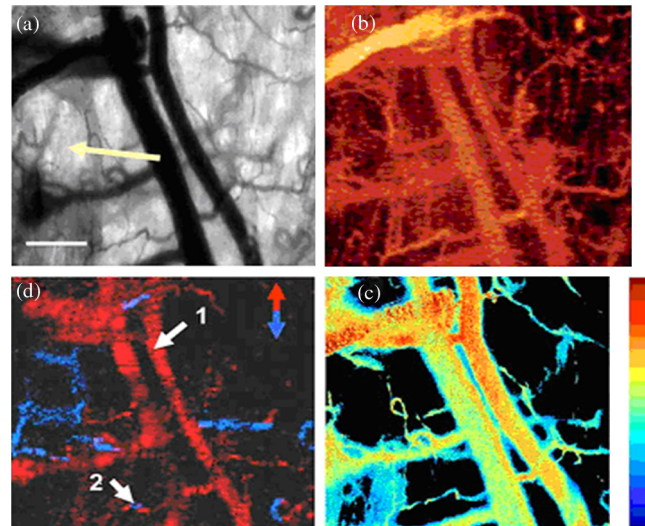


Fig. 8 SV imaging of a tumor vasculature in the dorsal skinfold mouse window chamber. (a) Transmission image taken with a tunable filter set at 500 nm. (b) SV-OCT image of vessel morphology. (c) Hyperspectral image of blood oxygen level (background pixels are black). (d) DOCT image of vessel blood flow direction. (Reproduced from Ref. 81 with permission.)

From initial case studies, the average volumetric vessel densities for scar and healthy region were equal to 12% and 8%, respectively. High concentrations of microvessels were observed in the scar region. In both images, the minimum detectable diameters of microvessels were found to be $\sim 30 \mu\text{m}$ under clinical conditions.

3.1.3 Imaging embryological tissue

Imaging the microvascular structure of the mammalian embryos has great potential for the study of cardiovascular birth defects and potential treatments. Recently, Sudheendran et al.⁸⁶ illustrated the vascular development in the cultured mouse embryos with the SV-OCT technique. The results showed that the embryonic yolk sac structure of the mouse undergoes significant changes at 8.5 and 9.5 days post coitus (dpc) similar to other embryonic cardiovascular studies.⁸⁷ The vasculature was clearly visible at both stages with apparent morphological difference found in the primitive vascular plexus at 8.5 dpc [Fig. 11(a)] and the remodeled hierarchically branching vascular network at 9.5 dpc [Fig. 11(b)].

For comparison, both DOCT and SV-OCT were used to reconstruct the same embryonic vascular structures (Fig. 12). The DOCT technique could not reconstruct several large vessels and capillaries in the central part of the image, where the embryonic yolk sac is perpendicular to the laser beam [Fig. 12(a)]. On the other hand, the corresponding SV-OCT technique provided more accurate representation of the vasculature of the yolk sac regardless of the flow direction [Fig. 12(b)]. In contrast, both methods outline vasculature equally well when blood flow has significant axial component [Fig. 12(c) and 12(d)]. Various colors in Doppler images represent the different directions of the axial flow components.

3.1.4 Applications in neuroscience

One of the most recent applications of the SV-OCT technique has been to visualize the intramedullary vasculature of the rodent

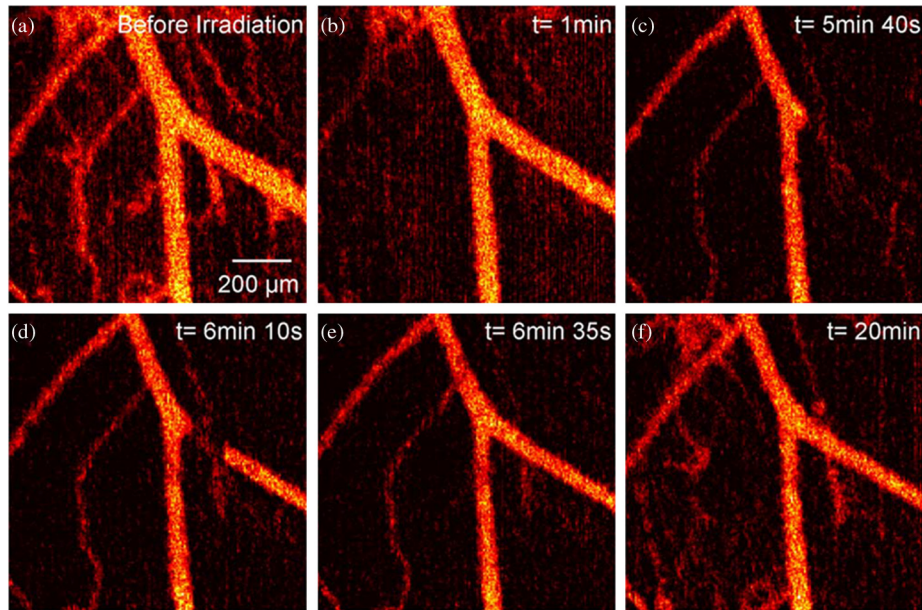


Fig. 9 SV-OCT imaging of PDT within the skinfold window chamber mouse model. (a) Vasculature prior to laser irradiation; (b) 1 min after laser irradiation; (c) total shutdown of right branch; (d) reperfusion of right branch with imaging artifact; (e) reperfusion of right branch without imaging artifact, and (f) 20 min laser irradiation showing reperfusion, but main vessels still appear to be constricted. Scale: 200 μm (Reproduced from Ref. 41 with permission.)

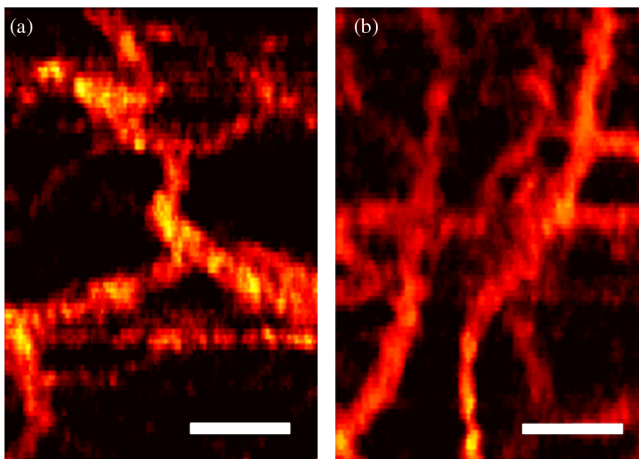


Fig. 10 *In vivo* SVOCT images of human oral tissue (a) in healthy region, (b) in scar (pathological) region. The increased number of microvasculature was seen in scar region. (Scale bar: 200 μm). (Reproduced from Ref. 85 with permission.)

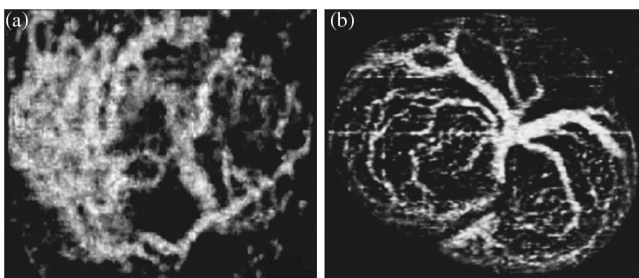


Fig. 11 Using the SV-OCT technique for imaging at different embryonic stages. (a) Nonremodeled vasculature (vascular plexus) of yolk sac vasculature at 8.5 dpc. (b) Remodeled yolk sac vasculature at 9.5 dpc. (Reproduced from Ref. 86 with permission.)

spinal cord, opening a plethora of opportunities for the neuroscience community. Cadotte et al.⁸⁸ successfully demonstrated the 3-D microvascular structure of the rodent spinal cord using the SV-OCT technique. In the case of imaging the spinal cord of a rat (Fig. 13), a spinal stabilizer was used to reduce the bulk cardio-respiratory motion. During a breath-hold cycle, structural OCT data were acquired [Fig. 13(b)]. The vascular imaging depth was found to be approximately 200 μm . The dorsal vein and its extensive tributaries can prevent microvascular imaging at deeper depth. While imaging the spinal cord of a mouse, less cardio-respiratory motion was observed, likely related to the different animal model used. A simple spinal stabilization jig was used to avoid bulk tissue motion. The structural OCT technique was capable of imaging approximately 500 μm into the mouse spinal cord, visualizing the entire dorsal gray matter and a portion of the ventral gray matter [Fig. 14(a)]. The SV-OCT and depth-dependent color mapping images are shown in Fig. 14(b) and 14(c), respectively. The diameter of the resolving microvessels in the mouse spinal cord was approximately 10 to 20 μm . By imaging a 3-D volume of tissue, this high temporal (μsec) and spatial resolution ($< 10 \mu\text{m}$) SV-OCT method offers the possibility of studying aspects of neurovascular coupling, whereby the optically invisible electrical events of neuronal signaling drive changes in the microvascular network to meet spatiotemporally isolated increases in metabolic requirements. While a host of other optical imaging techniques have been used to study the phenomenon of neurovascular coupling in the cerebral cortex, SV-OCT holds promise to uncover afferent or efferent stimulus-specific hemodynamic response functions in the spinal cord with high temporal resolution.

3.1.5 Tracing nanoparticles

Another aspect of the SV technique is that it may be used to trace the diffusion of nanoparticles (i.e., Au nanorings) in a sample and observe its systematical diffusion behaviors.⁸⁹ With

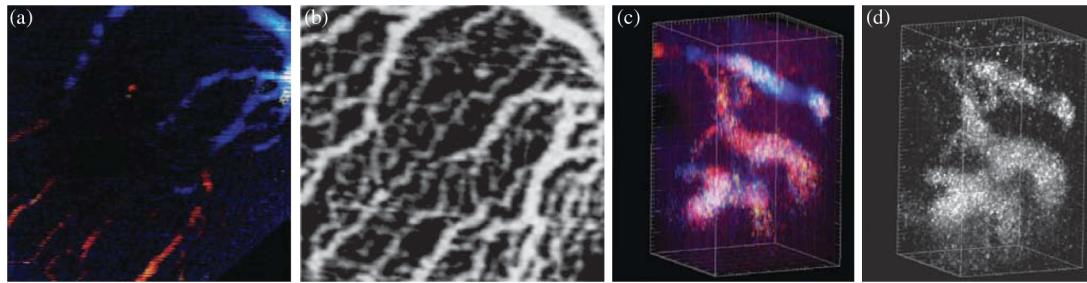


Fig. 12 3-D reconstruction of the embryonic yolk sac vasculature (a) with DOCT; (b) with SV-OCT analysis, exhibiting more structurally complex, clearly outlined vasculature; (c) 3-D reconstruction of the vasculature in the mouse embryonic brain acquired with DOCT; and (d) corresponding reconstruction acquired using SV analysis. (Reproduced from Ref. 86 with permission.)

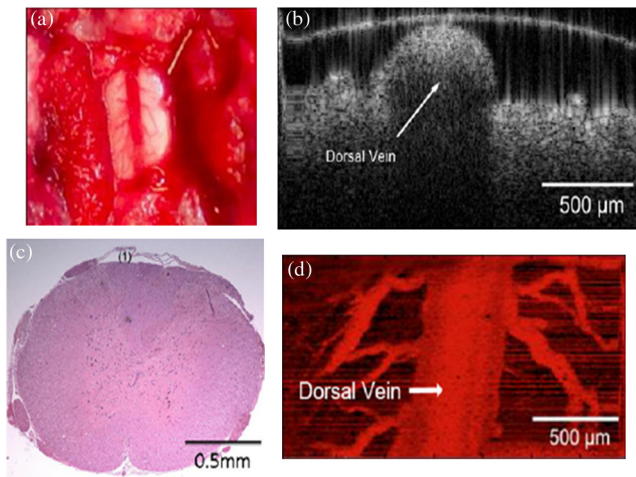


Fig. 13 (a) An exposed rat spinal cord. (b) Structural OCT image. (c) A histology specimen image was provided for comparison. (d) An *en-face* projection of the SV-OCT image. (Reproduced from Ref. 88 by Cadotte et al. with permission.)

resonant Au nanorings (Au-NRs), the distributions of nanorings were deeper inside the sample with time. However, with a high concentration of the Au-NRs solution, the overall localized surface plasmon resonance (LSPR) behavior became weaker than that of individual Au-NRs. As a result, the overall intensity of the OCT signal could appear attenuated, which limited further analysis from SVOCT. The technique's potential remains to be proven in future studies under physiologically tolerable Au-NR concentrations.

3.1.6 Application in ophthalmology

Another application of the SV technique is in the field of ophthalmology. For this purpose, Jia et al.⁴⁶ developed the split-spectrum amplitude-decorrelation (SSAD) algorithm, which has significantly improved the image contrast and allowed for the visualization of the microvasculature of the posterior part of the human eye. This method may be used to diagnose and/or treat blinding diseases such as glaucoma, diabetic retinopathy, and age-related macular degeneration. The algorithm consists of dividing the OCT spectrum into several spectral

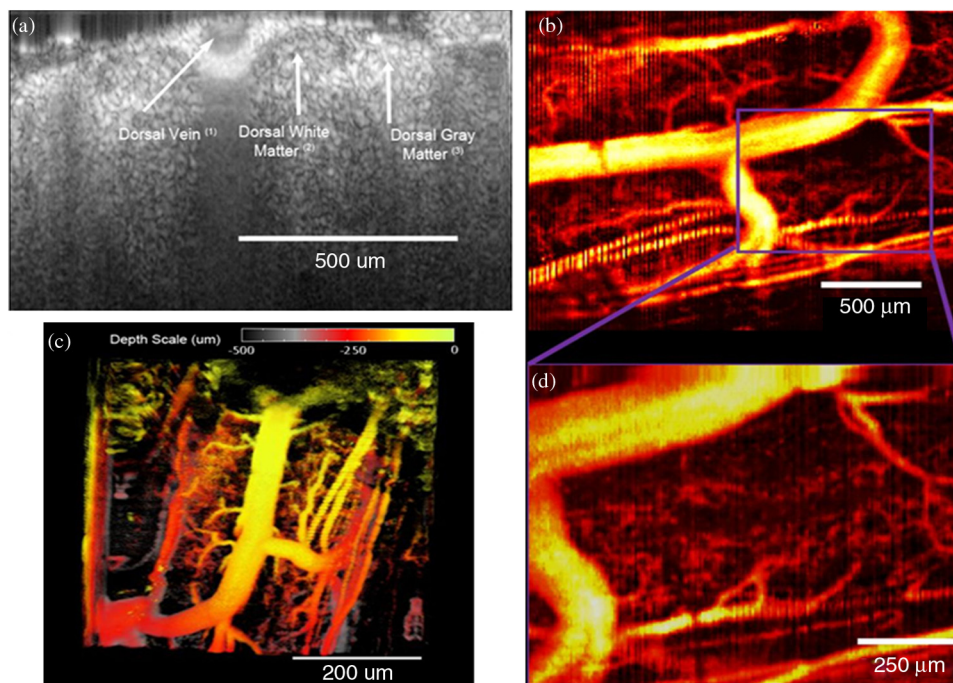


Fig. 14 Imaging the spinal cord of a mouse. (a) Structural OCT image, (b) SV-OCT images, (c) depth-dependent color mapping image, and (d) magnified selected box SV-OCT image. (Reproduced from Ref. 88 by Cadotte et al. with permission.)

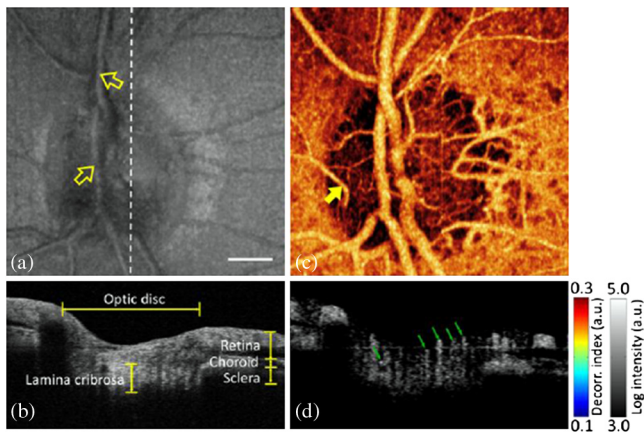


Fig. 15 *In vivo* 3-D volumetric ONH angiography. (a) *En face* reflectance intensity projection angiogram (yellow arrows point to major branches). (b) Vertical cross-section (B-mode) image marked with a dashed line in A. (c) *En face* decorrelation projection angiogram computed with the SSAD algorithm. The image showed central retinal blood vessels with various branches, a dense capillary network in the disc, a cilioretinal artery (yellow arrow), and a near continuous sheet of choroidal vessels around the disc. (d) Decorrelation cross-section (same plane as b) showed disc blood vessels (green arrows), peripapillary retinal vessels, and choroid. White bar: 500 μm . (Reproduced from Ref. 46 with permission.)

(wavenumber) bands and then calculates the inter-B-scan decorrelation of each of these spectral bands, both separately and averaged. The degradation in the axial resolution caused by splitting up the spectrum is a major drawback of this implementation. Figure 15 showed the *in vivo* optic nerve head (ONH) angiograms obtained by the reflectance intensity images and decorrelation images computed with SSAD algorithm. The *en face* reflectance intensity image [Fig. 15(a)] showed all major blood vessels; but capillaries and microvasculature of the retina, choroid, and optic disc were not visible during imaging. On the other hand, the *en face* decorrelation image [Fig. 15(c)] showed all major retinal vessels, as well as capillaries and the microvascular network of the ONH. Layers of tissue morphology, such as retina, choroid, and sclera, can be delineated in the OCT cross-section (B-mode) image [Fig. 15(b)]. In the decorrelation cross-section image [Fig. 15(d)], the disc blood vessels (marked with green arrows) were clearly visualized approximately 1.0 mm deep inside the disc. The SSAD algorithm was also tested on *in vivo* images of the human macula (Fig. 16). The vascular pattern and capillary networks and the foveal avascular zone (FAZ) were clearly visualized in the retinal circulation *en face* image [Fig. 16(a)]. In an ideal case, the vessel should not be present in the FAZ region; however, few false branches were found in this region due to noise.⁴⁶ Previous studies suggested that the choriocapillaris layer develops a confluent overlapping plexus; therefore, an *en face* decorrelation image of the choroid circulation [Fig. 16(b)] showed confluent flow. The cross-sectional OCT images [Fig. 16(c) and 16(d)] of the retinal vessels [marked with upper and lower dashed lines in Fig. 16(a)] showed different tissue layers from the nerve fiber layer (NFL) to the outer plexiform layer.

3.2 Applications of PV-OCT

PV-OCT is widely used to create vascular maps of human eyes.^{47,61–66} Kim et al.^{61,64,65} demonstrated the feasibility of a

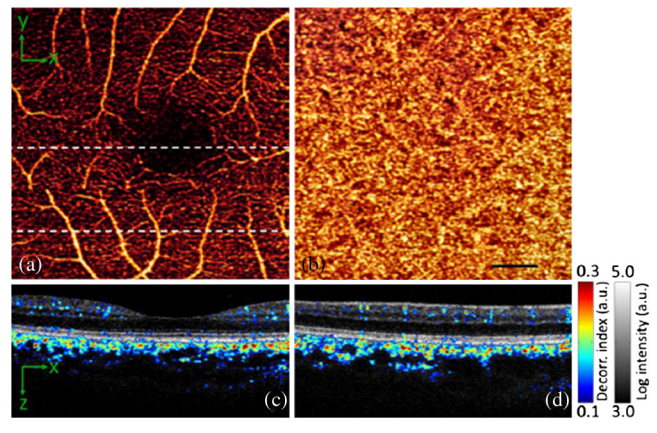


Fig. 16 *En face* decorrelation projection angiogram of the retina (a) and the choroidal (b) circulation processed with the SSAD algorithm. (c) OCT image through the foveal center (upper dashed line in a). (d) OCT image of the inferior macula (lower dashed line in a). Black bar: 500 μm . (Reproduced from Ref. 46 with permission.)

high-speed PV-OCT system for 2-D visualization of the capillary network over the foveal and perifoveal regions, as well as 3-D representation of the vasculature in the human retina. A spectral domain OCT system (at center wavelength ~ 850 nm, 125,000 lines/s with 2048 pixels) was used for the PV measurement. The scanning protocols used a series of BM-scans (here “BM-scans” means that it takes multiple B-scans over time for the same transverse scan region) acquired across the fovea, with each BM-scan consisting of three successive B-scans at the same location. The imaging acquisition time of PV-OCT is 3.5 s. Phase differences between sequential B-scans were extracted for PV contrast calculation. The imaging results were shown in Fig. 17.

The size of the smallest resolvable capillary detected from this acquisition scheme is 10 to 12 μm . PV-OCT shows details of capillary networks comparable to the gold standard fundus FA imaging. In addition, PV-OCT provides depth information of capillary locations. They also imaged multiple volumes and vascular maps to visualize a larger region of the retina, demonstrating potential for realistic clinical applications. The stitched vascular map and fundus FA are shown in Fig. 18. Depth-resolved color maps are shown in Fig. 18(b). Such PV-OCT imaging may be useful to improve the early diagnosis of retinal vascular diseases, including diabetic retinopathy and vascular-related macular degeneration.

Furthermore, Kim et al.⁷⁸ also demonstrated *en face* visualization of human retinal microcirculation using average intensity OCT, SV-OCT, PV-OCT, and FA. The fundus FA photo of the magnified foveal region is shown in Fig. 19(a), and 2-D projection images generated by the average intensity projection of the retina is presented in Fig. 19(b). The bright spot (marked as a red dotted circle) in the center of the foveal region in Fig. 19(c) is the back-reflection signal from the central fovea. The *en face* projection image of the entire retina achieved by PV-OCT [Fig. 19(d)] shows similar results as the image from SV-OCT method [Fig. 19(c)], excluding two horizontal stripes (marked as red arrows).

There is an important need to enhance the imaging depth for capturing both retinal and choroidal microvasculatures. PV-OCT systems at a 850-nm central wavelength offer good resolution and sensitivity for retinal imaging, but longer wavelengths may improve imaging of the deeper choroidal vessels.

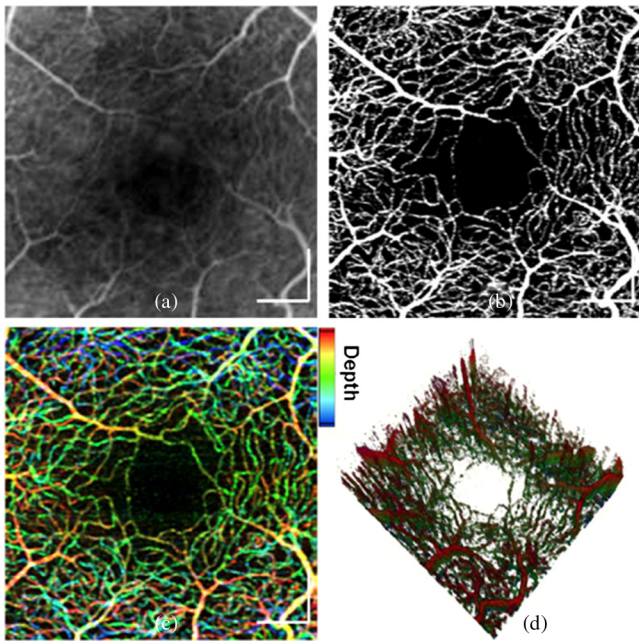


Fig. 17 Retinal perfusion images of the parafoveal region. (a) FA image. (b) Projection view of PV-OCT. (c) Color-coded depth projection view of PV-OCT. (d) 3-D color depth-coded image of PV-OCT. Colors in depth: superficial layer, red; intermediate layer, green; deep layer, blue. Scale bar: 300 μm . (Reproduced from Ref. 65 with permission.)

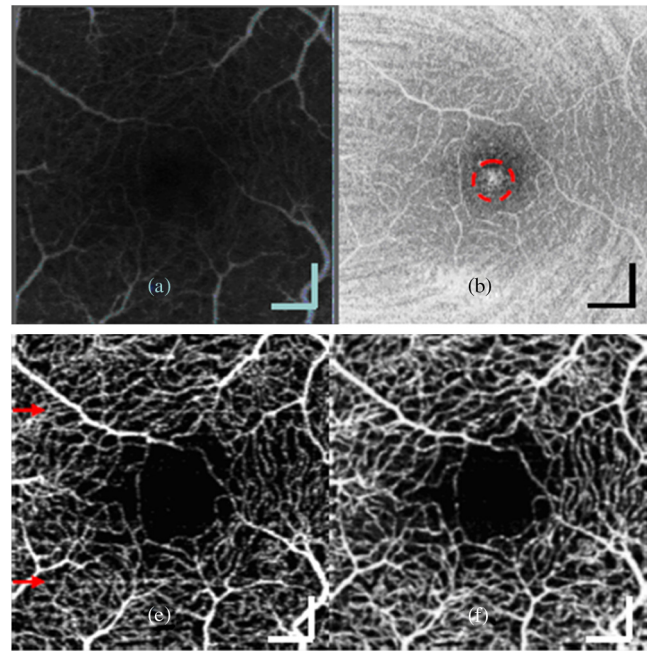


Fig. 19 Retinal perfusion network of foveal region of the entire inner retina. (a) Fundus FA image. (b) *En-face* average intensity-based OCT image. (c) *En-face* SV-OCT images. Two red arrows mark the position of bulk motions during acquisition. (d) *En face* PV-OCT image. Scale bar: 300 μm . (Reprinted from Ref. 64 with permission.)

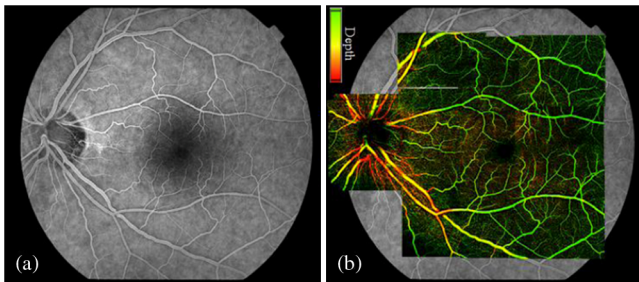


Fig. 18 (a) FA image. (b) PV-OCT vascular map of the retina acquired from 10 volumes and overlaid on fundus FA. (Reproduced from Ref. 61 with permission.)

Swept-source OCT systems at a 1000-nm central wavelength with a 50-kHz line-rate (A-scan) has been developed.^{62,63} With an OCT system at a 1,300-nm central wavelength, the phase contrast method can image vasculature in the brain and tumors, but it is not the ideal choice for ophthalmic imaging due to the significant absorption by the vitreous. Therefore, based on the intended purpose of imaging, different OCT systems should be applied to specific applications.

Unlike the phase processing methods, including DOCT and PV-OCT, the SV method allows for a simple acquisition and post-processing algorithm and shows less sample motion artifacts effects and vessel shadows in the axial direction;⁶⁶ however, this method produces low-contrast images of the vascular network due to the bright NFL and inner retinal structures. The SV-OCT method demonstrates similar microvascular maps with the FA and the PV-OCT when scanned over the central foveal region. However, SV values from the microcapillaries in the NFL and below the thick NFL lacked sufficient SNRs for reliable visualization of microcirculation in these regions. This

is in contrast to PV-OCT methods, which visualized microcapillaries and larger vessels from the OCT-scanned volumes without such limitations. PV-OCT with rapid image acquisition at a high-speed A-scan rate can help to reduce acquisition time and related eye motion artifacts.

Recently, Liu et al.^{36,80} developed a modified Doppler variance algorithm that is based on the intensity (or amplitude) information rather than on phase information. Performances of this intensity-based Doppler variance (IBDV) method were compared to the traditional phase-resolved Doppler variance (PRDV) and phase-resolved color Doppler (PRCD) methods while mapping vascular network and extraction of blood vessel information.³⁶ PRCD is most sensitive when flow direction is along the probing beam. Both PRDV and IBDV are better to measure blood flow when the flow direction is nearly perpendicular to the probing beam. However, PRDV and IBDV show Doppler angle-dependent behavior above a certain angle (> 12 deg). In applications where microvascular mapping (such as angiogram) is more important than the flow velocity quantification, both IBDV and PRDV images are high-contrast images and can detect smaller blood vessels (capillary) than that of PRCD images. However, the IBDV method is less sensitive to bulk motion with relatively simple post-processing steps, which is preferred for fast data processing.

Another alternative method known as correlation mapping OCT (cmOCT) has been developed to map vasculature networks and the blood flow information from the OCT images.^{90,91} The technique is capable of extracting blood flow information without the need of phase information. In addition, the system does not require any modification of the exiting OCT hardware. Parameters such as capillary density, vessel location, and diameter can be detected using this technique. The minimum detectable diameter of the microvessel volar forearm was achieved at about 33 μm .⁹⁰ Although the system can image

the microvascular structures, the exact locations of these vessels within the tissue were found previously. Further studies are necessary to improve this technique.

4 Discussion and Conclusions

In conclusion, we have reviewed the principles, algorithms, and applications of two microcirculation imaging techniques: SV- and PV-OCT, and compared their performances to DOCT and other gold standard techniques. The PV-OCT method can visualize vasculature structure independent of the vessel orientation and the flow velocity. However, this method is phase-sensitive; therefore, a highly phase-stable optical system is necessary. With a high-speed A-scan acquisition rate (in the kilohertz to megahertz range), B-scan image size and imaging speed can be increased to realize 3-D phase-variance contrast imaging more efficiently. Several potential applications of the PV technique are *in vivo* high-contrast vasculature imaging of the human retina for diagnosis of the ocular diseases, brain tissue vasculature, and study of vasculature in tumors/cancer cells. Further improvements of this technique require the minimization of shadowing artifacts, necessary to full 3-D, large-volume imaging of high-resolution microvasculature networks.

The SV-OCT is another attractive technique of detecting, quantifying, and monitoring microcirculation. Unlike DOCT and PV-OCT, SV methods are not phase-resolved, instead relying on the comparisons of consecutive structural (A-scan or B-scan) OCT images. This method is advantageous for detecting microvasculature because of its sensitivity, Doppler angle-independent microvascular information with little additional computational complexity and fast imaging technique. Lower data storage requirements relative to PV microvascular imaging techniques add further utility to this technique. Despite promising results, this technique also suffers from multiple scattering-induced blood vessel shadowing artifacts^{47,48} and susceptible to bulk tissue motion,⁴¹ which causes high interframe variance. High A-scan imaging systems, which ensure a sufficient number of acquired frames for calculation of speckle decorrelation, can diminish the bulk motion artifacts.^{50,92} Further study is necessary to overcome the limitations of accurately quantifying blood flow information.⁸¹

We summarized both SV- and PV-OCT technologies in terms of algorithms and their applications for microvasculature imaging. In comparison to other vascular-sensitive OCT imaging methods, both of these techniques have unique strengths and weaknesses that make them useful in different preclinical and clinical situations. Neither is categorically superior to the other, and both require ongoing methodological improvements specific to the research question at hand.

Acknowledgments

The authors thank the Canadian Institutes of Health Research (CIHR), Natural Sciences and Engineering Council, and Ryerson Bio-photonics and Bioengineering Laboratory for funding contributions. Dr. David Cadotte is supported by a CIHR Health Professional Fellowship award.

References

- J. Gass, *Stereoscopic Atlas of Macular Diseases: Diagnosis and Treatment*, 4th ed., Vol. 2, Mosby, St. Louis, Missouri (1997).
- D. Huang et al., "Optical coherence tomography," *Science* **254**(5035), 1178–1181 (1991).
- A. F. Fercher et al., "In vivo optical coherence tomography," *Am. J. Ophthalmol.* **116**(1), 113–114 (1993).
- S. Yazdanfar, M. Kulkarni, and J. Izatt, "High-resolution imaging of *in vivo* cardiac dynamics using color Doppler optical coherence tomography," *Opt. Express* **1**(13), 424–431 (1997).
- Z. Chen et al., "Noninvasive imaging of *in vivo* blood flow velocity using optical Doppler tomography," *Opt. Lett.* **22**(14), 1119–1121 (1997).
- S. Yazdanfar, A. M. Rollins, and J. A. Izatt, "Imaging and velocimetry of the human retinal circulation with color Doppler optical coherence tomography," *Opt. Lett.* **25**(19), 1448–1450 (2000).
- V. Westphal et al., "Real-time, high velocity-resolution color Doppler optical coherence tomography," *Opt. Lett.* **27**(1), 34–36 (2002).
- R. Leitgeb et al., "Real-time assessment of retinal blood flow with ultra-fast acquisition by color Doppler Fourier domain optical coherence tomography," *Opt. Express* **11**(23), 3116–3121 (2003).
- B. R. White et al., "In vivo dynamic human retinal blood flow imaging using ultra-high-speed spectral domain optical Doppler tomography," *Opt. Express* **11**(25), 3490–3497 (2003).
- L. Wang et al., "Frequency domain phase-resolved optical Doppler and Doppler variance tomography," *Opt. Commun.* **242**(4–6), 345–350 (2004).
- B. J. Vakoc et al., "Three-dimensional microscopy of the tumor micro-environment *in vivo* using optical frequency domain imaging," *Nat. Med.* **15**(10), 1219–1223 (2009).
- T. Schmoll, C. Kolbitsch, and R. A. Leitgeb, "Ultra-high-speed volumetric tomography of human retinal blood flow," *Opt. Express* **17**(5), 4166–4176 (2009).
- I. V. Larina et al., "Hemodynamic measurements from individual blood cells in early mammalian embryos with Doppler swept source OCT," *Opt. Lett.* **34**(7), 986–988 (2009).
- M. Bonesi, S. Matcher, and I. Meglinski, "Doppler optical coherence tomography in cardiovascular applications," *Laser Phys.* **20**(6), 1491–1499 (2010).
- I. V. Larina et al., "Live imaging of blood flow in mammalian embryos using Doppler swept-source optical coherence tomography," *J. Biomed. Opt.* **13**(6), 060506 (2008).
- J. a. Izatt et al., "In vivo bidirectional color Doppler flow imaging of picoliter blood volumes using optical coherence tomography," *Opt. Lett.* **22**(18), 1439–1441 (1997).
- Y. Zhao et al., "Phase-resolved optical coherence tomography and optical Doppler tomography for imaging blood flow in human skin with fast scanning speed and high velocity sensitivity," *Opt. Lett.* **25**(2), 114 (2000).
- S. Yazdanfar, A. M. Rollins, and J. A. Izatt, "In vivo imaging of human retinal flow dynamics by color Doppler optical coherence tomography," *Arch. Ophthalmol.* **121**(2), 235–239 (2003).
- S. Makita, M. Yamanari, and Y. Yasuno, "High-speed and high-sensitive optical coherence angiography," *Proc. SPIE* **7372**, 73721M (2009).
- S. Zotter et al., "Visualization of microvasculature by dual-beam phase-resolved Doppler optical coherence tomography," *Opt. Express* **19**(2), 1217–1227 (2011).
- S. Makita et al., "Comprehensive *in vivo* micro-vascular imaging of the human eye by dual-beam-scan Doppler optical coherence angiography," *Opt. Express* **19**(2), 1271–1283 (2011).
- C. J. Pedersen et al., "Phase-referenced Doppler optical coherence tomography in scattering media," *Opt. Lett.* **30**(16), 2125–2127 (2005).
- M. Szkulmowski et al., "Flow velocity estimation using joint spectral and time domain optical coherence tomography," *Opt. Express* **16**(9), 6008–6025 (2008).
- H. Ren et al., "Power optical Doppler tomography imaging of blood vessel in human skin and M-mode Doppler imaging of blood flow in chick chorioallantoic membrane," *Proc. SPIE* **4956**, 225–231 (2003).
- V. Yang et al., "High speed, wide velocity dynamic range Doppler optical coherence tomography (Part I): system design, signal processing, and performance," *Opt. Express* **11**(7), 794–809 (2003).
- H. Ren et al., "Real-time *in vivo* blood-flow imaging by moving scatterer-sensitive, spectral-domain optical Doppler tomography," *Opt. Lett.* **31**(7), 927–929 (2006).
- S. Makita et al., "Optical coherence angiography," *Opt. Express* **14**(17), 7821–7840 (2006).
- T.-T. Chi et al., "Motion-insensitive optical coherence tomography based micro-angiography," *Opt. Express* **19**(27), 26117–26131 (2011).

29. R. K. Wang et al., "Optical microangiography provides depth-resolved images of directional ocular blood perfusion in posterior eye segment," *J. Biomed. Opt.* **15**(2), 020502 (2010).
30. H. M. Subhash et al., "Volumetric *in vivo* imaging of microvascular perfusion within the intact cochlea in mice using ultra-high sensitive optical microangiography," *IEEE Trans. Med. Imag.* **30**(2), 224–230 (2011).
31. H. Ren and X. Li, "Clutter rejection filters for optical Doppler tomography," *Opt. Express* **14**(13), 6103–6112 (2006).
32. S. Yousefi, Z. Zhi, and R. Wang, "Eigendecomposition-based clutter filtering technique for optical micro-angiography," *IEEE Trans. Biomed. Eng.* **58**(8), 2316–2323 (2011).
33. F. Jaillon et al., "Enhanced imaging of choroidal vasculature by high-penetration and dual-velocity optical coherence angiography," *Biomed. Opt. Express* **2**(5), 1147–1158 (2011).
34. L. An, J. Qin, and R. K. Wang, "Ultrasound sensitive optical microangiography for *in vivo* imaging of microcirculations within human skin tissue beds," *Opt. Express* **18**(8), 8220–8228 (2010).
35. R. K. Wang et al., "Depth-resolved imaging of capillary networks in retina and choroid using ultrahigh sensitive optical microangiography," *Opt. Lett.* **35**(9), 1467–1469 (2010).
36. G. Liu et al., "A comparison of Doppler optical coherence tomography methods," *Biomed. Opt. Express* **3**(10), 56–60 (2012).
37. R. K. Wang and L. An, "Doppler optical micro-angiography for volumetric imaging of vascular perfusion *in vivo*," *Opt. Express* **17**(11), 8926–8940 (2009).
38. L. An and R. K. Wang, "*In vivo* volumetric imaging of vascular perfusion within human retina and choroids with optical micro-angiography," *Opt. Express* **16**(15), 11438–11452 (2008).
39. L. An, T. T. Shen, and R. K. Wang, "Using ultrahigh sensitive optical microangiography to achieve comprehensive depth resolved microvasculature mapping for human retina," *J. Biomed. Opt.* **16**(10), 106013 (2011).
40. J. Barton and S. Stromski, "Flow measurement without phase information in optical coherence tomography images," *Opt. Express* **13**(14), 5234–5239 (2005).
41. A. Mariampillai et al., "Speckle variance detection of microvasculature using swept-source optical coherence tomography," *Opt. Lett.* **33**(13), 1530–1532 (2008).
42. A. Mariampillai et al., "Optimized speckle variance OCT imaging of microvasculature," *Opt. Lett.* **35**(8), 1257–1259 (2010).
43. L. Conroy, R. S. Dacosta, and I. A. Vitkin, "Quantifying tissue microvasculature with speckle variance optical coherence tomography," *Opt. Lett.* **37**(15), 3180–3182 (2012).
44. X. Liu et al., "Spectroscopic-speckle variance OCT for microvasculature detection and analysis," *Biomed. Opt. Express* **2**(11), 2995–3009 (2011).
45. X. Liu et al., "Quantitative transverse flow measurement using optical coherence tomography speckle decorrelation analysis," *Opt. Lett.* **38**(5), 805–807 (2013).
46. Y. Jia et al., "Split-spectrum amplitude-decorrelation angiography with optical coherence tomography," *Opt. Express* **20**(4), 3116–3121 (2012).
47. J. Fingler et al., "Volumetric microvascular imaging of human retina using optical coherence tomography with a novel motion contrast technique," *Opt. Express* **17**(24), 22190–22200 (2009).
48. V. J. Srinivasan et al., "Rapid volumetric angiography of cortical microvasculature with optical coherence tomography," *Opt. Lett.* **35**(1), 43–45 (2010).
49. M. Szkulmowski, et al., "Efficient reduction of speckle noise in optical coherence tomography," *Opt. Express* **20**(2), 1337–1359 (2012).
50. K. K. C. Lee et al., "Real-time speckle variance swept-source optical coherence tomography using a graphics processing unit," *Biomed. Opt. Express* **3**(7), 1557–1564 (2012).
51. Y. Zhao et al., "Doppler standard deviation imaging for clinical monitoring of *in vivo* human skin blood flow," *Opt. Lett.* **25**(18), 1358–1360 (2000).
52. H. Ren et al., "Phase-resolved functional optical coherence tomography: simultaneous imaging of *in situ* tissue structure, blood flow velocity, standard deviation, birefringence, and Stokes vectors in human skin," *Opt. Lett.* **27**(19), 1702–1704 (2002).
53. B. Park et al., "Real-time fiber-based multi-functional spectral-domain optical coherence tomography at 1.3 μm ," *Opt. Express* **13**(11), 3931–3944 (2005).
54. Y. Zhao et al., "Three-dimensional reconstruction of *in vivo* blood vessels in human skin using phase-resolved optical Doppler tomography," *IEEE J. Sel. Top. Quant. Electron.* **7**(6), 931–935 (2001).
55. H. Ren et al., "Imaging and quantifying transverse flow velocity with the Doppler bandwidth in a phase-resolved functional optical coherence tomography," *Opt. Lett.* **27**(6), 409–411 (2002).
56. Z. Ding et al., "Real-time phase-resolved optical coherence tomography and optical Doppler tomography," *Opt. Express* **10**(5), 236–245 (2002).
57. J. Zhang and Z. Chen, "*In vivo* blood flow imaging by a swept laser source-based Fourier domain optical Doppler tomography," *Opt. Express* **13**(19), 7449–7457 (2005).
58. B. Vakoc et al., "Phase-resolved optical frequency domain imaging," *Opt. Express* **13**(14), 5483–5493 (2005).
59. J. Fingler et al., "Mobility and transverse flow visualization using phase variance contrast with spectral domain optical coherence tomography," *Opt. Express* **15**(20), 12636–12653 (2007).
60. J. Fingler et al., "Phase-contrast OCT imaging of transverse flows in the mouse retina and choroid," *Invest. Ophthalmol. Vis. Sci.*, **49**(11), 5055–5059 (2008).
61. D. Y. Kim et al., "*In vivo* volumetric imaging of human retinal circulation with phase-variance optical coherence tomography," *Biomed. Opt. Express* **2**(6), 1504–1513 (2011).
62. R. Motaghianezam and S. Fraser, "*In vivo* human retinal and choroidal vasculature visualization using differential phase contrast swept source optical coherence tomography at 1060 nm," *Proc. SPIE* **8213**, 821304 (2012).
63. S. M. R. Motaghianezam, D. Koos, and S. E. Fraser, "Differential phase-contrast, swept-source optical coherence tomography at 1060 nm for *in vivo* human retinal and choroidal vasculature visualization," *J. Biomed. Opt.* **17**(2), 026011 (2012).
64. D. Y. Kim et al., "Noninvasive imaging of the foveal avascular zone with high-speed, phase-variance optical coherence tomography," *Invest. Ophthalmol. Vis. Sci.* **53**(1), 85–92 (2012).
65. D. Y. Kim et al., "Visualization of human retinal micro-capillaries with phase contrast high-speed optical coherence tomography," *Proc. SPIE* **7889**, 78890H (2011).
66. T. Schmoll et al., "Imaging of the parafoveal capillary network and its integrity analysis using fractal dimension," *Biomed. Opt. Express* **2**(5), 1159–1168 (2011).
67. J. M. Schmitt, S. H. Xiang, and K. M. Yung, "Speckle in optical coherence tomography," *J. Biomed. Opt.* **4**(1), 95–105 (1999).
68. M. Bashkansky and J. Reintjes, "Statistics and reduction of speckle in optical coherence tomography," *Opt. Lett.* **25**(8), 545–547 (2000).
69. B. Karamata et al., "Speckle statistics in optical coherence tomography," *J. Opt. Soc. Am. A* **22**(4), 593–596 (2005).
70. G. Lamouche et al., "Speckle size in optical coherence tomography," *Proc. SPIE* **6627**, 66270R (2007).
71. A. F. Fercher, "Inverse scattering, dispersion, and speckle in optical coherence tomography," in *Biological and Medical Physics, Biomedical Engineering*, pp. 119–146, Springer-Verlag, Berlin, Heidelberg (2008).
72. V. Yang et al., "High frequency ultrasound speckle flow imaging comparison with Doppler optical coherence tomography (DOCT)," in *Proc. IEEE Ultrasonics Symposium*, Vol. 1, pp. 453–456, IEEE, Ontario, Canada (2004).
73. W. Aoudi et al., "Estimation methods for flow imaging with high-frequency ultrasound," *Ultrasonics* **44**(Suppl. 1), e135–e140 (2006).
74. J. W. Goodman, *Statistical Optics*, Vol. 1, pp. 361–465, Wiley, New York (1985).
75. V. X. D. Yang et al., "Improved phase-resolved optical Doppler tomography using the Kasai velocity estimator and histogram segmentation," *Opt. Commun.* **208**(4–6), 209–214 (2002).
76. A. Mariampillai, "Development of a high-resolution microvascular imaging toolkit for optical coherence tomography," PhD Thesis, University of Toronto (2010).
77. C. Kasai et al., "Real-time two-dimensional blood flow imaging using an autocorrelation technique," *IEEE Trans. Sonics Ultrasonics* **32**(3), 458–464 (1985).
78. D. Y. Kim et al., "Visualization of human retinal capillary networks: a comparison of intensity, speckle-variance and phase-variance optical coherence tomography," *Proc. SPIE* **8213**, 821307 (2012).
79. L. Yu and Z. Chen, "Doppler variance imaging for three-dimensional retina and choroid angiography," *J. Biomed. Opt.* **15**(1), 016029 (2010).

80. G. Liu et al., "Intensity-based modified Doppler variance algorithm: application to phase instable and phase stable optical coherence tomography systems," *Opt. Express* **19**(12), 11429–11440 (2011).
81. M. C. Skala et al., "Combined hyperspectral and spectral domain optical coherence tomography microscope for noninvasive hemodynamic imaging," *Opt. Lett.* **34**(3), 289–291 (2009).
82. A. Vitkin, "Improving treatment efficacy with biological and biophysical feedback," *SPIE Newsroom*, 4–7 (2012).
83. H. A. Collins et al., "Blood-vessel closure using photosensitizers engineered for two-photon excitation," *Nat. Photon.* **2**(7), 420–424 (2008).
84. A. Maeda et al., "In vivo optical imaging of tumor and microvascular response to ionizing radiation," *PloS One* **7**(8), e42133 (2012).
85. B. Davoudi et al., "Noninvasive in vivo structural and vascular imaging of human oral tissues with spectral domain optical coherence tomography," *Biomed. Opt. Express* **3**(5), 826–839 (2012).
86. N. Sudheendran et al., "Speckle variance OCT imaging of the vasculature in live mammalian embryos," *Laser Phys. Lett.* **8**(3), 247–252 (2011).
87. J. L. Lucitti et al., "Vascular remodeling of the mouse yolk sac requires hemodynamic force," *Development* **134**(18), 3317–3326 (2007).
88. D. W. Cadotte et al., "Speckle variance optical coherence tomography of the rodent spinal cord: in vivo feasibility," *Biomed. Opt. Express* **3**(5), 911–919 (2012).
89. C.-K. Lee et al., "Characterizing the localized surface plasmon resonance behaviors of Au nanorings and tracking their diffusion in bio-tissue with optical coherence tomography," *Opt. Express* **1**(4), 1060–1073 (2010).
90. E. Jonathan, J. Enfield, and M. J. Leahy, "Correlation mapping method for generating microcirculation morphology from optical coherence tomography (OCT) intensity images," *J. Biophoton.* **4**(9), 583–587 (2011).
91. J. Enfield, E. Jonathan, and M. Leahy, "In vivo imaging of the microcirculation of the volar forearm using correlation mapping optical coherence tomography (cmOCT)," *Opt. Express* **2**(5), 1184–1193 (2011).
92. A. Mariampillai et al., "Doppler optical cardiogram gated 2D color flow imaging at 1000 fps and 4D in vivo visualization of embryonic heart at 45 fps on a swept source OCT system," *Opt. Express* **15**(4), 1627–1638 (2007).